



Article

Facile Microwave Production and Photocatalytic Activity of Bismuth Vanadate Nanoparticles over the Acid Orange 7

Nataša Tot ^{1,*}, Bojana Vasiljević ¹, Slađana Davidović ², Anđela Pustak ³, Ivan Marić ³, Ivan Marić ³, Ivan Prekodravac Filipović ¹, and Dragana Marinković ^{1,*}

- Vinča Institute of Nuclear Sciences, National Institute of the Republic of Serbia, University of Belgrade, P.O. Box 522, 11001 Belgrade, Serbia; bojana.vasiljevic@vin.bg.ac.rs (B.V.); prekodravac@vin.bg.ac.rs (J.P.F.)
- Department of Biochemical Engineering and Biotechnology, Faculty of Technology and Metallurgy, University of Belgrade, Karnegijeva 4, 11000 Belgrade, Serbia; sdavidovic@tmf.bg.ac.rs
- Radiation Chemistry and Dosimetry Laboratory, Ruder Bošković Institute, Bijenička Cesta 54, 10 000 Zagreb, Croatia; apustak@irb.hr (A.P.); imaric@irb.hr (I.M.)
- * Correspondence: natasa.tot@vin.bg.ac.rs (N.T.); draganaj@vin.bg.ac.rs (D.M.)

Abstract

This work reports the rapid aqueous microwave-assisted synthesis of monoclinic scheelite BiVO₄ nanoparticles and their behavior under visible light. X-ray diffraction (XRD) confirms phase-pure BiVO₄ with an average crystallite size of ~19 nm, consistent with transmission electron microscopy (TEM) observations, while N₂ sorption yields a BET surface area of 7.5 m²/g. UV–Vis diffuse reflectance spectroscopy (DRS) indicates a direct band gap of 2.55 eV. We evaluated the effects of catalyst dosage and initial Acid Orange 7 (AO7) concentration on visible-light degradation efficiency. Up to 77% removal was achieved within 120 min, with kinetics following a pseudo-first-order model (R² \approx 0.970–0.996). Under the tested conditions, BiVO₄ also exhibited a modest antibacterial effect against *Escherichia coli* (~0.5 log reduction). These findings demonstrate that microwave-synthesized BiVO₄ is a multifunctional material and provides a quantitative baseline for practical wastewater treatment studies under visible light.

Keywords: Bismuth vanadate (BiVO₄); microwave-assisted synthesis; energy band gap; visible-light photocatalysis; Acid Orange 7; antibacterial properties; wastewater treatment



Academic Editor: Andrea Petrella

Received: 2 October 2025 Revised: 21 October 2025 Accepted: 25 October 2025 Published: 30 October 2025

Citation: Tot, N.; Vasiljević, B.; Davidović, S.; Pustak, A.; Marić, I.; Prekodravac Filipović, J.; Marinković, D. Facile Microwave Production and Photocatalytic Activity of Bismuth Vanadate Nanoparticles over the Acid Orange 7. Processes 2025, 13, 3485. https://doi.org/10.3390/pr13113485

Copyright: © 2025 by the authors. Licensee MDPI, Basel, Switzerland. This article is an open access article distributed under the terms and conditions of the Creative Commons Attribution (CC BY) license (https://creativecommons.org/licenses/by/4.0/).

1. Introduction

Water represents a key natural resource essential for life support, human health, and ecosystem balance. However, rising living standards are often accompanied by increased industrial production and consumption, which lead to excessive pollution of water, air, and soil [1]. The presence of pollutants such as pesticides, heavy metals, and pharmaceuticals in the environment can cause severe ecological and public health risks [2].

Among various contaminants in aquatic ecosystems, organic dyes pose significant environmental concern because of their extensive industrial application in textiles, leather, paper, food processing, and cosmetics [3,4]. Within this group, azo dyes are the most widely used, accounting for more than 60% of all synthetic dyes produced worldwide [5]. They are characterized by one or more azo bonds, which provide high chemical stability, strong color intensity, and remarkable resistance to light, temperature, and microbial degradation [5,6]. While these properties are desirable in industrial applications, they also make azo dyes persistent in the environment. Moreover, their degradation products, including aromatic amines, are often toxic, mutagenic, or carcinogenic to humans and aquatic life [7]. A

Processes 2025, 13, 3485 2 of 15

representative of this group is AO7, an anionic azo dye widely used in textile dyeing and paper printing. Its complex aromatic structure makes AO7 resistant to conventional wastewater treatment methods, which poses a major environmental challenge [8].

Conventional water purification approaches, including coagulation, activated carbon adsorption, reverse osmosis, ultrafiltration, and biological treatments, are frequently insufficient for the effective elimination of these pollutants [9]. As a result, advanced oxidation processes (AOPs) have attracted considerable attention for the degradation of azo dyes, particularly AO7 [8,10]. These processes generate reactive oxygen species (ROS) capable of mineralizing pollutants into non-toxic end products such as CO₂, water, and inorganic ions [11]. Within this context, heterogeneous photocatalytic processes have achieved significant progress, distinguished by their environmental compatibility and demonstrated efficiency in wastewater treatment and air purification [12,13].

Titanium dioxide (TiO_2) is the most extensively investigated photocatalyst due to its stability and low toxicity. However, its 3.0–3.2 eV band gap confines activity to the UV range (\approx 5% of the solar spectrum) [14,15]. Accordingly, recent studies have focused on visible-light-responsive photocatalysts, which are capable of harvesting a larger fraction of solar energy [16]. Among visible-light photocatalysts, BiVO₄ stands out owing to its narrower band gap (\sim 2.4 eV) and robust chemical/photostability, while being accessible by straightforward syntheses [17–19]. Its electronic structure, involving O 2p and Bi 6s hybrid orbitals, facilitates visible-light absorption more efficiently than TiO_2 , whose valence band consists only of O 2p orbitals [20]. The monoclinic scheelite phase of BiVO₄ is recognized for superior photocatalytic activity compared to tetragonal forms, mainly due to its narrower band gap and favorable charge-transport properties. This has been repeatedly demonstrated in azo-dye degradation under visible-light irradiation [21,22].

The performance of BiVO₄ can be improved through material modifications that increase light absorption and limit charge recombination. As reported for Eu³⁺ doping, the lifetime of photoexcited electrons was extended, enabling ~90% degradation of Methyl Orange in 180 min under visible irradiation [23]. Heterojunction formation has also proven highly effective. BiVO₄/TiO₂ composite achieved complete degradation of Acid Blue 113 in just 20 min [24], while AgBr-decorated BiVO₄ reached ~93% removal of AO7 in 80 min under visible-light irradiation [25].

Beyond its photocatalytic activity, BiVO₄ has also been recognized as exhibiting antibacterial effects toward Escherichia coli, primarily through mechanisms involving the generation of ROS and the resulting oxidative stress that compromises cellular membranes and essential biomolecules [17,26]. Microwave-synthesized BiVO₄ nanoparticles have been reported to inhibit the growth of *Escherichia coli*, thereby indicating concurrent photocatalytic and antibacterial activity in aqueous systems [26–28]. Furthermore, tetragonal zircon-type BiVO₄ nanoparticles (2–8 nm) obtained via an ethylene glycol-assisted method were reported to induce severe bacterial cell wall damage, which was attributed to the synergistic effect of ROS formation and electrostatic interactions between positively charged Bi³⁺ surface sites and negatively charged bacterial membranes [29,30].

Collectively, these results underscore the potential of ${\rm BiVO_4}$ as a multifunctional material capable of simultaneously enabling pollutant degradation and efficient microbial inactivation, which is of particular importance for integrated water treatment and disinfection applications.

Considering these favorable properties, this study aims to synthesize, characterize, and evaluate the photocatalytic and antibacterial performance of $BiVO_4$ nanoparticles prepared through a rapid, low-cost, and environmentally friendly microwave-assisted route. This method provides uniform heating, short reaction time, and improved energy efficiency. The obtained $BiVO_4$ samples were characterized by XRD to determine crystal

Processes 2025, 13, 3485 3 of 15

structure and crystallite size, TEM to assess morphology and particle distribution, BET analysis to evaluate specific surface area and porosity, and FTIR to identify vibrational features. To evaluate the photocatalytic performance, AO7 degradation experiments were carried out under visible light at the unadjusted pH, varying both the catalyst dosage and initial dye concentration. Furthermore, the antibacterial activity of BiVO₄ nanoparticles was tested against a representative bacterial strain, demonstrating their dual functionality and potential application in integrated wastewater treatment and disinfection systems.

2. Materials and Methods

2.1. Materials

Acid Orange 7(AO7)

Unless otherwise stated, all reagents were of analytical grade, purchased from Merck (Darmstadt, Germany), and used without further purification. Table 1 summarizes the main chemicals applied in the synthesis and photocatalytic experiments.

95% (dye grade)

633-96-5

Reagent Name	Chemical Formula	Purity	CAS No.
Bismuth nitrate pentahydrate	$Bi(NO_3)_3 \times 5H_2O$	≥99% (AR)	10035-06-0
Ammonium metavanadate	NH_4VO_3	99%	7803-55-6
Nitric acid	HNO_3	>99% (AR)	7697-37-2

Table 1. The main chemical reagents used in the experiments.

C₁₆H₁₁N₂NaO₄S

2.2. Synthesis of BiVO₄

BiVO₄ was obtained through a microwave-assisted aqueous synthesis. Bismuth nitrate pentahydrate (Bi(NO₃)₃ × 5H₂O, 5.0 mL, 0.05 M) and ammonium metavanadate (NH₄VO₃, 5.5 mL, 0.05 M) were dissolved separately and then combined in a G30 reaction vial containing a magnetic stir bar, giving a total reaction volume of 10.5 mL. The initial pH of the combined precursor solution was approximately 4.5, determined prior to microwave heating and attributable to Bi³⁺ hydrolysis in the nitrate medium. The mixed solution was stirred for 5 min to ensure uniformity before the vial was closed with a septum and standard cap. The synthesis was conducted in a mono-mode Anton Paar microwave reactor (Anton Paar GmbH, Graz, Austria) under temperature-controlled conditions at 170 °C for 10 min. During the heating phase, the reactor applied up to 300 W of microwave power, reaching the set temperature in about 1 min, and the internal pressure stabilized near 26 bar, within the 30 bar operating limit. After natural cooling to room temperature, the product dispersion was centrifuged at 12,000 rpm for 20 min, and the collected solid was rinsed three times with deionized water and ethanol. No pH adjustment or mineralizing agent was introduced at any step. The washed material was vacuum-dried at 70 °C for 180 min, yielding a pale-yellow, phase-pure monoclinic BiVO₄ powder with approximately 98% recovery. Preliminary optimization on the same reactor confirmed that 170 °C for 10 min reproducibly produced pure BiVO₄, while longer or hotter programs did not alter the XRD phase composition.

2.3. Characterization

XRD measurements were carried out on a Bruker diffractometer (Cu K α , 40 kV, 30 mA; Bruker, Billerica, MA, USA). Diffraction data were collected at room temperature over a 2 θ range of 10–70°, using a scanning speed of 3° min⁻¹ and a 0.5 mm divergent slit. The

Processes 2025, 13, 3485 4 of 15

average crystallite size was calculated from the most intense diffraction peak according to the Scherrer equation (Equation (1)):

$$D = \frac{k\lambda}{\beta \cos\theta} \tag{1}$$

where D is the crystallite size, k is the shape factor, λ is the wavelength, β is the FWHM, and θ is the Bragg angle.

TEM images were obtained using an FEI Tecnai F20 microscope (FEI, Hillsboro, OR, USA) operated at 200 kV after drop-casting the sample dispersion onto lacey carbon grids.

The textural properties of the material were examined by nitrogen adsorption–desorption isotherms recorded at 77 K using a Quantachrome Autosorb iQ3 analyzer (Quantachrome Instruments, Boynton Beach, FL, USA). Prior to measurement, samples were vacuum-degassed by gradual heating until the pressure stabilized below 50 mTorr/min, indicating complete removal of adsorbed gases and moisture. Specific surface area was determined via BET analysis (p/ $p_0 = 0.05$ –0.30), and pore characteristics were derived from the shape of the isotherm.

FTIR spectroscopy was carried out on a Thermo Scientific Nicolet iS50 (Thermo Fisher Scientific, Waltham, MA, USA) spectrometer equipped with a built-in all-reflective ATR diamond accessory. Spectra were recorded in the range of 400–4000 cm $^{-1}$ with a spectral resolution of 4 cm $^{-1}$ at room temperature.

The optical properties were evaluated by UV–Vis DRS using a Shimadzu 1800 spectrophotometer (Shimadzu, Kyoto, Japan) equipped with an integrating sphere in the wavelength range of 300–800 nm. The reflectance data were converted into absorbance using the Kubelka–Munk function (Equation (2)):

$$F(R) = \frac{(1-R)^2}{2R}$$
 (2)

where R is the observed reflectance.

The optical band gap (Eg) was then estimated according to the Tauc relation (Equation (3)):

$$F(FKM(R) \times hv)^{1/n} = A(hv - Eg)$$
(3)

where $F_{KM}(R)$ is the Kubelka–Munk function, R is the observed reflectance in the UV–Vis spectrum, $h\nu$ is the photon energy, A is a proportionality constant, and n characterizes the electronic transition type. Assuming a direct-allowed transition (n = 1/2), Eg was extracted from the linear portion of $(F(R) h\nu)^2$ vs. $h\nu$ extrapolated to $(F(R) h\nu)^2 = 0$.

2.4. Evaluation of Photocatalytic Activity

The photocatalytic performance of BiVO₄ was evaluated by degrading Acid Orange 7 (AO7) in aqueous solution under visible-light irradiation. A 300 W Osram Vitalux lamp was positioned ~30 cm above the reactor, providing broadband emission across the UV–visible–IR range (UVB 280–315 nm: 3.0 W; UVA 315–400 nm: 13.6 W). The incident irradiance at the liquid surface was ~30 mW cm⁻², measured with an R-752 universal radiometer equipped with a PH-30 (DIGIRAD) sensor. All tests were performed in a sealed reactor under these standardized conditions. To convey measurement precision, the kinetic plots include standard deviation (SD) error bars reflecting the estimated experimental uncertainty (\approx 2–3%).

 $\rm BiVO_4$ (10, 15, or 20 mg) was dispersed in 50 mL of AO7 solution (15–25 ppm) and magnetically stirred. After a 60 min dark-equilibration period to minimize initial adsorption transients, the suspension was irradiated. A photolysis blank (identical irradiation, no catalyst) was run in parallel.

Processes **2025**, 13, 3485 5 of 15

At predefined times (up to 120 min), 1.5 mL aliquots were withdrawn, clarified by centrifugation (12,000 rpm, 20 min), and analyzed by UV–Vis spectroscopy. AO7 concentration was tracked at its absorption maximum ($\lambda_{max} \approx 484$ nm), and the temporal decay of C/C₀ was used to follow decolorization kinetics.

The degradation efficiency (D) was calculated using Equation (4):

$$D(\%) = \frac{C_0 - C_t}{C_0} \times 100 \tag{4}$$

where C_0 represents the initial concentration of AO7, while C_t corresponds to the concentration after irradiation for time.

The photocatalytic degradation kinetics were analyzed according to the Langmuir–Hinshelwood pseudo-first-order model (Equation (5)):

$$-ln\left(\frac{C_t}{C_0}\right) = Kt \times t \tag{5}$$

where Kt is the apparent pseudo-first-order rate constant.

2.5. Antibacterial Properties

Antimicrobial activity of the BiVO₄ nanoparticles was examined against the Gramnegative bacterium *Escherichia coli* ATCC 25922. An overnight culture of *E. coli* was prepared in tryptic soy broth (Torlak, Belgrade, Serbia) supplemented with 0.6% yeast extract (Torlak, Serbia). The culture was centrifuged, washed twice with sterile physiological saline (0.9% NaCl), and resuspended to a final concentration of approximately 10^7 CFU/mL. Afterwards, $100~\mu$ L of the bacterial suspension was added to $9.9~\mu$ L of a BiVO₄ nanoparticle suspension (1 mg/mL), which had been previously irradiated with UV light for 30 min to enhance photocatalytic activity. The sample was incubated at $37~\mu$ C with shaking at $120~\mu$ C rpm for 4 h, in parallel with a control (*E. coli* without BiVO₄). Following incubation, serial decimal dilutions were prepared and plated on sterile tryptic soy agar (TSA) plates. The plates were incubated for $24~\mu$ at $37~\mu$ C, after which colony-forming units (CFU) were counted. The percentage of bacterial growth inhibition was calculated as follows (Equation (6)):

$$R(\%) = \frac{C_0 - C}{C_0} \times 100 \tag{6}$$

where C_0 is the number of CFU from the control sample and C is the number of CFU from the treated sample.

The experiment was performed in triplicate and statistical analysis of the results was performed using OriginPro (OriginLab Corporation, Northampton, MA, USA). One-way analysis of variance (ANOVA), followed by Tukey's test, was used to determine statistical significance. A p-value of p < 0.05 was considered statistically significant.

3. Results and Discussion

3.1. Structural and Morphological Properties of the Microwave-Synthesized BiVO₄

Figure 1 shows the structural and morphological characterization of the synthesized BiVO₄ powder. The XRD pattern (Figure 1a) matches the JCPDS 01-074-4894 reference, confirming single-phase monoclinic scheelite (clinobisvanite, space group I2/b). The main reflections at $2\theta \approx 18.9^{\circ}$, 28.9° , 30.5° , 35.2° , and 39.7° correspond to the (011), (112), (004), (020), and (211) planes of monoclinic BiVO₄, respectively, indicating a highly crystalline, phase-pure material obtained by microwave-assisted synthesis. The average crystallite size, estimated from the most intense peak at $2\theta \approx 28.9^{\circ}$ using the Scherrer equation, was ~19 nm, consistent with TEM results.

Processes 2025, 13, 3485 6 of 15

TEM (Figure 1b) further reveals nanosized particles with a relatively uniform distribution and an average size of ~20 nm, in agreement with the XRD-derived crystallite size (~19 nm). Most nanoparticles are near-spherical to slightly irregular—typical of microwave-assisted rapid nucleation and growth [17,20]. The TEM also indicates that the majority of the particles are discrete, although some degree of agglomeration can be observed, which is commonly reported for BiVO₄ nanoparticles owing to their high surface energy [21,26]. The ~19–20 nm crystallite size, together with high phase purity, shortens carrier migration paths and mitigates bulk recombination, which supports the visible-light activity reported later, despite the modest BET surface area.

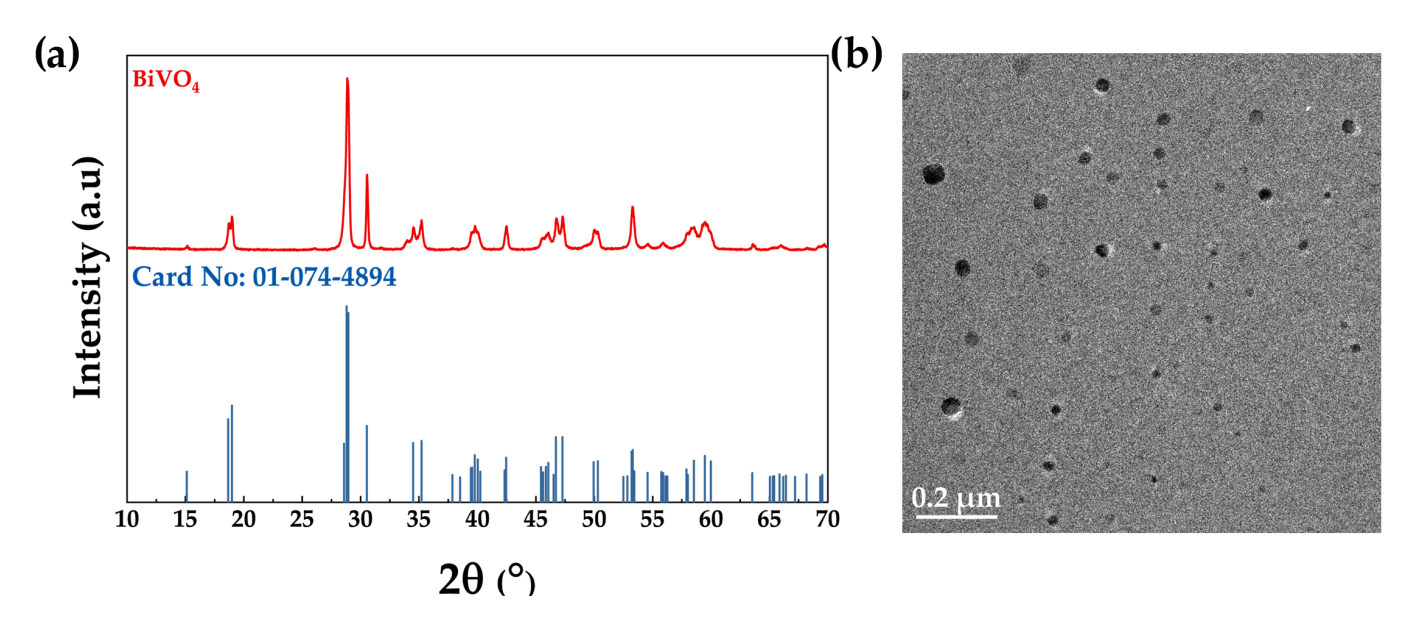


Figure 1. (a) XRD pattern of BiVO₄ with reference bars (card No: 01-074-4894); (b) TEM image of BiVO₄ nanoparticles.

3.2. Textural, Vibrational, and Optical Properties of the Microwave-Synthesized BiVO₄

Figure 2 summarizes the textural and vibrational characterization. The N_2 adsorption-desorption isotherm (Figure 2a) corresponds to IUPAC Type II with negligible hysteresis, consistent with a non-porous to weakly porous compact powder [17,31]. The BET-specific surface area is 7.5 m²/g, a value typical of dense, microwave-synthesized BiVO₄ and indicative of limited external porosity [17]. In such systems, photocatalytic performance is governed primarily by visible-light harvesting and charge-carrier dynamics rather than by surface area. The ~20 nm crystallite size shortens e^-/h^+ migration paths, reduces bulk recombination, and thereby mitigates the influence of the modest BET value [19]. Numerous reports document that materials with relatively low SBET can still deliver satisfactory activity when charge separation and transport are efficient [24]. Related BiVO₄ systems with structural or morphological control likewise show moderate visible-light performance at modest surface areas, attributed to nanoscale ordering, morphology tuning, and defect-assisted charge separation [24,25].

The FTIR spectrum (Figure 2b) displays well-resolved bands characteristic of monoclinic scheelite BiVO₄. Features at ~805 and ~603 cm⁻¹ are assigned to asymmetric and symmetric stretching modes of VO₄³⁻ units, while the band near ~510 cm⁻¹ arises from Bi–O vibrations [17,19]. No additional absorptions are observed in the 800–1200 cm⁻¹ and 1400–1700 cm⁻¹ regions, excluding common phosphate/silicate/carbonate impurities; a weak signal at ~1380 cm⁻¹ is consistent with trace nitrates from precursors [19]. Taken together, the sharp internal vibrations and the absence of extraneous bands corroborate phase purity and a well-ordered VO₄ framework, in agreement with XRD/TEM. Such structural

Processes 2025, 13, 3485 7 of 15

ordering is conducive to efficient charge-carrier separation with mitigated recombination, supporting the satisfactory visible-light activity observed despite the modest SBET [24]. Finally, the direct band gap of 2.55 eV positions BiVO₄ for efficient visible-light harvesting while maintaining sufficient oxidizing power. Combined with nanoscale crystallites, this balance enables interfacial charge transfer and underpins the first-order-like behavior within the L–H window reported in Section 3.3.

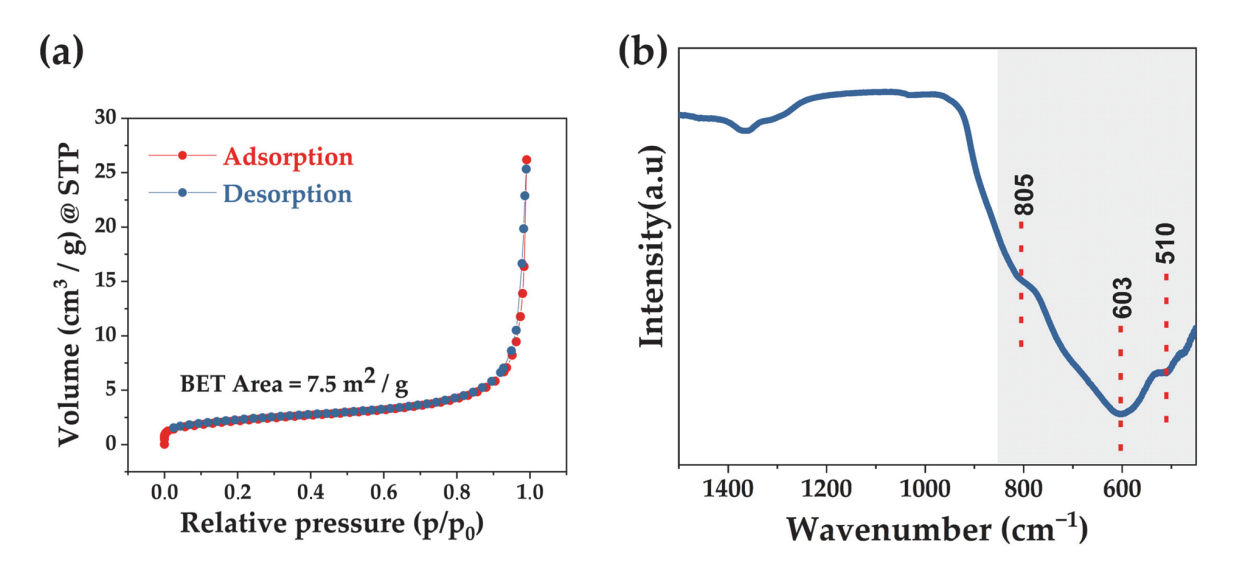


Figure 2. Textural and vibrational characterization of $BiVO_4$: (a) N_2 adsorption–desorption isotherm; (b) FTIR spectrum.

Eg was determined from the Tauc plot (Equations (2) and (3)) assuming a direct-allowed transition giving 2.55 eV (Figure 3). This value is consistent with reported monoclinic BiVO $_4$ (\approx 2.4–2.6 eV) [17]. The consistency of the obtained result with the literature further corroborates the formation of a pure monoclinic scheelite phase, as confirmed by XRD, and underlines the semiconductor's suitability for visible-light-driven photocatalytic applications. The band gap position ensures efficient utilization of the solar spectrum while maintaining sufficient oxidative potential, thus providing a favorable balance between light absorption and redox activity.

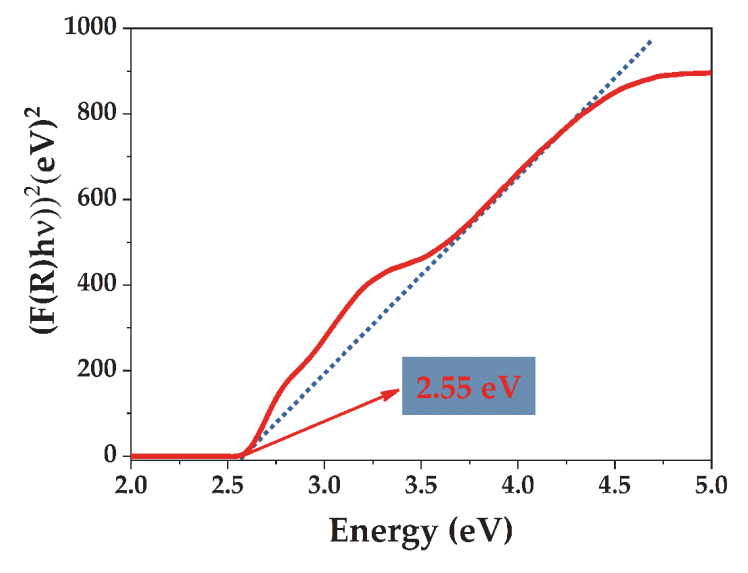


Figure 3. Tauc's plot for BiVO₄ from Kubelka–Munk-transformed UV–Vis DRS; the linear fit of (F(R) $h\nu$)² vs. $h\nu$ extrapolated to (F(R) $h\nu$)² = 0 yields and Eg = 2.55 eV (direct, n = 1/2).

Processes 2025, 13, 3485 8 of 15

3.3. Photocatalytic Performance of the Microwave-Synthesized BiVO₄

AO7 in aqueous solution served as the model pollutant to evaluate the visible-light photocatalytic activity of BiVO₄. Prior to irradiation, dye–catalyst suspensions were magnetically stirred in the dark for 60 min to reach adsorption–desorption equilibrium; the concentration after this step was taken as C_0 . A blank conducted under identical visible-light irradiation but without BiVO₄ showed only ~10% AO7 loss over 120 min, indicating minimal direct photolysis. Accordingly, the decreases observed under irradiation in the presence of BiVO₄ are attributed to photocatalytic conversion rather than adsorption or photolysis. The influences of catalyst dosage and initial dye concentration are examined below; pH was not systematically adjusted and remained near its native value (~4.5).

The direct band gap (2.55 eV) enables visible-light absorption, while \sim 19–20 nm crystallites shorten carrier migration paths and facilitate interfacial charge transfer. Under the native pH, dye–surface electrostatics together with light-utilization constraints govern the observed trends in the apparent rate constant k with dosage and initial AO7 concentration. These factors rationalize the increase in k with catalyst mass up to 15–20 mg and its higher value at lower AO7 loads.

3.3.1. The Effect of Catalyst Dosage on the Degradation of Acid Orange 7

Figure 4 shows the time-resolved UV–Vis spectra of AO7 under visible-light irradiation in the presence of 15 mg BiVO₄, with a slight hypsochromic shift (λ max \approx 484 nm). The shoulder within 440–520 nm progressively collapses, while the near-UV features around 250–320 nm attenuate more slowly, consistent with the stepwise loss of conjugation in the dye chromophore [32].

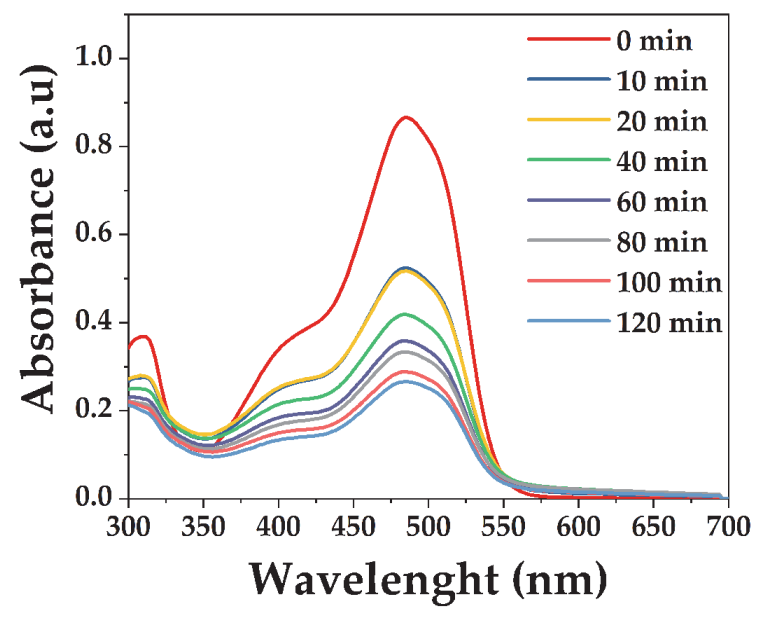


Figure 4. UV-Vis absorption spectra of the AO7 solution (20 ppm) for 15 mg of BiVO₄.

Figure 5 shows the effect of BiVO₄ dosage on AO7 degradation and the temporal decay of C/C₀ at 484 nm. Figure 5a presents the temporal decay of the normalized concentration (C/C₀) at the absorption maximum of AO7 (λ max \approx 484 nm). In the absence of BiVO₄, only about 10% of AO7 was removed after 120 min, confirming that the degradation is primarily photocatalyst-driven. Increasing the catalyst dosage from 10 to 15 mg markedly enhanced degradation efficiency, with ~68% removal compared to ~55% for the lower loading. A further increase to 20 mg resulted in only a slight additional improvement, reaching ~72% after 120 min, indicating that the system operates close to its optimum catalyst loading.

Processes 2025, 13, 3485 9 of 15

The corresponding pseudo-first-order kinetic plots (Figure 5b) exhibit good linearity, consistent with the Langmuir–Hinshelwood model. The calculated rate constants increased with catalyst dosage, being lowest for 10 mg and highest for 20 mg, although the difference between 15 and 20 mg remained relatively small. This trend reflects a balance between the number of active surface sites and the efficiency of light utilization. At higher dosages, more reactive sites are available; however, excessive amounts can lead to light scattering, shielding effects, and partial particle aggregation, which ultimately limit further improvements in photocatalytic activity [33,34].

Based on these results, a dosage of 15 mg BiVO₄ was used to study the effect of initial AO7 concentration, balancing efficiency and avoiding high-loading drawbacks.

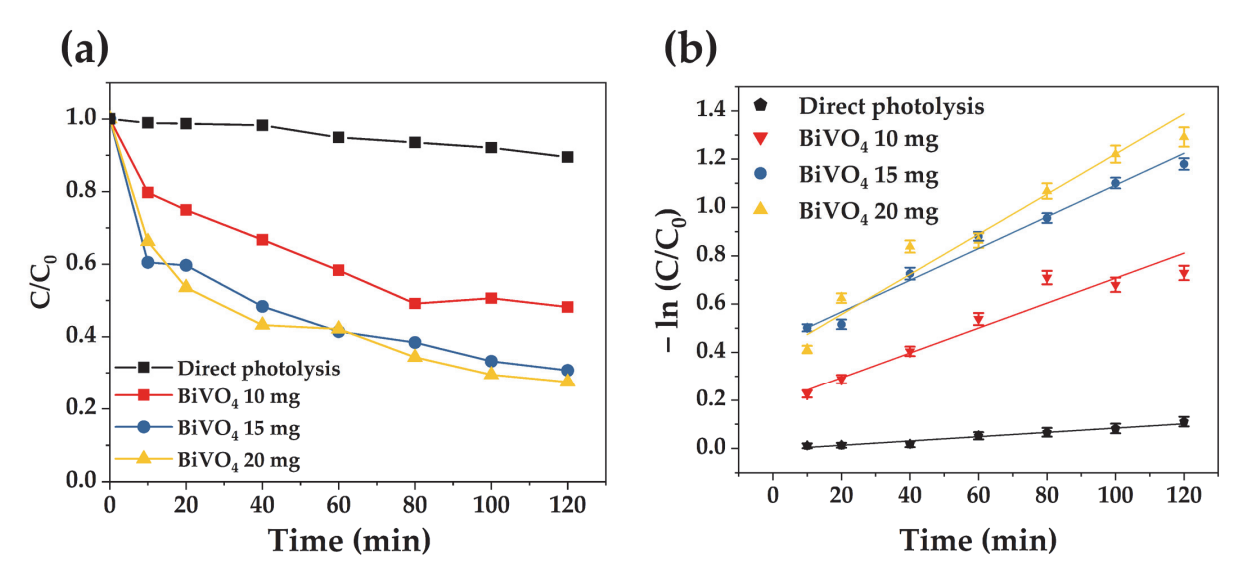


Figure 5. Effect of BiVO₄ catalyst dosage on the photocatalytic degradation of AO7 (20 ppm) under visible-light irradiation, including direct photolysis are as follows: (a) temporal decay of normalized concentration (C/C_0) with time; (b) pseudo-first-order kinetic plots with SD error bars.

3.3.2. Influence of the Initial Acid Orange 7 Concentration on Visible-Light Photodegradation Performance

After establishing 15 mg BiVO $_4$ as the optimal catalyst dosage, the effect of the initial AO7 concentration was investigated. Figure 6a shows that the degradation efficiency decreases with increasing dye concentration. At 15 ppm, about 77% of AO7 was removed within 120 min, while the efficiency declined to ~69% at 20 ppm and ~70% at 25 ppm. This reduction is associated with stronger coloration of the solution at higher concentrations, which limits light penetration, as well as the saturation of active sites by excess dye molecules, reducing the availability of reactive oxygen species for photocatalytic reactions [35–37].

Kinetic plots (Figure 6b) follow pseudo-first-order kinetics, with linear fits yielding apparent rate constants of $0.00983~\rm min^{-1}$ for 15 ppm, $0.00963~\rm min^{-1}$ for 20 ppm, and $0.00811~\rm min^{-1}$ for 25 ppm. The higher value obtained at 15 ppm indicates that the reaction proceeds faster at lower pollutant loads, while the decrease in k with increasing concentration reflects competition among dye molecules for both photons and active sites. Correlation coefficients ($R^2 > 0.95$) further support the applicability of the Langmuir–Hinshelwood kinetic model (Table 2) [38,39].

Processes 2025, 13, 3485 10 of 15

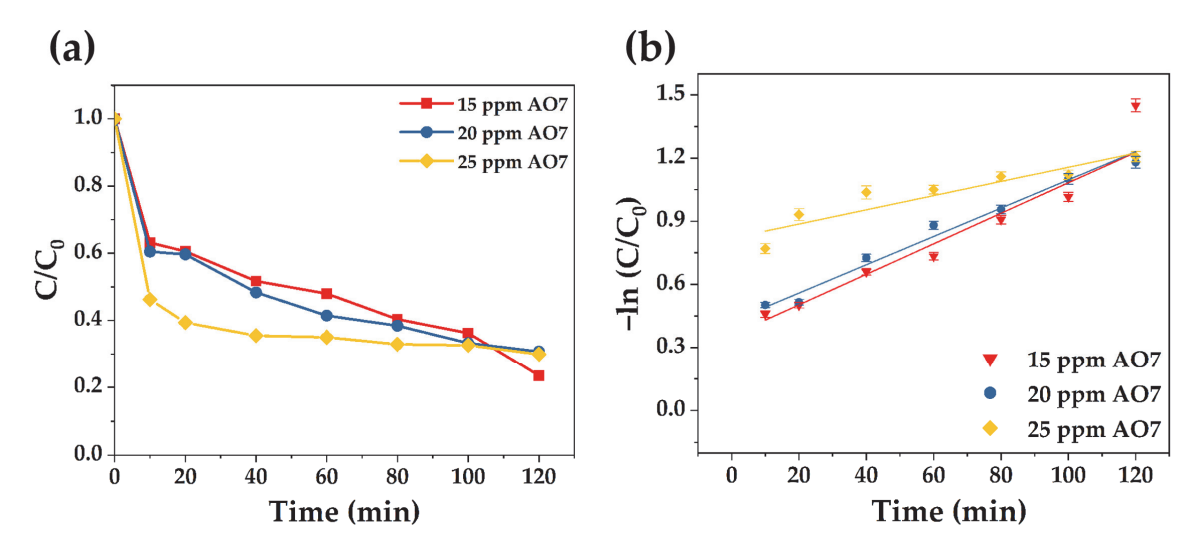


Figure 6. Effect of initial AO7 concentration (15 ppm, 20 ppm, and 25 ppm) on the photocatalytic degradation over BiVO₄ (15 mg) under visible-light irradiation are as follows: (a) temporal decay of normalized concentration (C/C_0) with time; (b) pseudo-first-order kinetic plots with SD error bars.

The kinetic parameters extracted from the pseudo-first-order fits are compiled in Table 2, allowing side-by-side comparison across both series (mass and concentration).

Table 2. Apparent rate constants (k) and correlation coefficients (R^2) for AO7 degradation over BiVO₄ under visible light.

Run	AO7 (ppm)	Catalyst Mass (mg)	k (min ⁻¹)	R ²		
Mass series at AO7 = 20 ppm						
m_1	20	10	0.00635	0.967		
m_2	20	15	0.00963	0.996		
m_3	20	20	0.01036	0.989		
Concentration series at mass 15 mg						
C_1	15	15	0.00983	0.995		
C_2	20	15	0.00963	0.996		
C_3	25	15	0.00811	0.983		

In comparison with conventional TiO₂ P25, the superior visible-light response of BiVO₄ becomes evident. Because of its wide band gap (~3.2 eV), TiO₂ P25 primarily absorbs UV light and typically exhibits very low apparent rate constants (k < 1 \times 10⁻³ min⁻¹) under visible-only irradiation [11,14]. In contrast, reported values for BiVO₄ during azo-dye degradation commonly fall within (8 \times 10⁻³)–(1.5 \times 10⁻²) min⁻¹, depending on morphology, synthesis route, and interfacial design [17,19]. Heterojunctions (e.g., BiVO₄/TiO₂) and plasmonic or metal modifications (e.g., Ag–BiVO₄) further improve charge separation and kinetics. The present microwave-synthesized BiVO₄ is consistent with these observations, as summarized in Table 3.

Table 3. Comparison of pseudo-first-order rate constants (k) and experimental conditions for dye degradation under visible light over TiO_2 P25 and $BiVO_4$ -based photocatalysts.

Photocatalyst	Pollutant	m (mg)	C ₀ (ppm)	Light Source	k (min ⁻¹)	Ref.
TiO ₂ P25	Acid Orange 7	100	10	10 W white LEDs (visible)	0.0016	[40]
TiO ₂ P25	Methylene Blue	100	10	500 W halogen	0.0036	[41]
$BiVO_4$	Acid Orange 7	15	20	300 W Osram Vitalux lamp	0.00963	This work
BiVO ₄	Mordant Blue 9	100	10	300 W solar simulator	0.0126	[21]

Processes 2025, 13, 3485 11 of 15

Table 3. Cont.

Photocatalyst	Pollutant	m (mg)	C ₀ (ppm)	Light Source	${ m k}$ (min $^{-1}$)	Ref.
BiVO ₄ /TiO ₂	Acid Blue 113	1000	40	1.6 kW Xe lamp	0.083	[24]
Eu/BiVO ₄	Methyl Orange	200	10	500 W Xe lamp	0.0039	[23]
Ag/BiVO ₄	Methylene Blue	100	10	Visible light ($\lambda \ge 420$ nm)	0.031	[22]
Ag/BiVO ₄	Rhodamine B	100	10	Visible light ($\lambda \ge 420 \text{ nm}$)	0.023	[22]

3.4. Possible Photocatalytic Pathway for the Degradation of Acid Orange 7

Figure 7 outlines a plausible route for AO7 degradation on visible-light-active BiVO₄. Upon irradiation, photoexcited electron–hole pairs generate reactive oxygen species (${}^{\bullet}$ O₂, ${}^{\bullet}$ OH) in parallel with direct hole oxidation (h⁺). Azo-bond cleavage initiates the sequence, which proceeds along two principal trajectories. On the benzene-derived branch, sulfonated aromatic amines evolve through stepwise oxidation to sulfonated hydroxybenzenes and, after desulfonation, to benzoic acid-type derivatives. On the naphthalene-derived branch, hydroxylated intermediates form and convert into additional hydroxylated naphthalenes, quinone species, and ultimately benzoic acid-type compounds. Prolonged oxidation on both branches plausibly promotes aromatic ring opening to low-molecular-weight aliphatic carboxylic acids and, in late stages, mineralization [10,32]. The sequence in Figure 7 accords with our spectral trends—most notably the attenuation of the 484 nm chromophore band—and with mechanisms reported for AO7 and structurally related azo dyes [42].

Figure 7. Plausible visible-light-driven AO7 degradation mechanism over BiVO₄, from azo-bond cleavage to oxidation intermediates and lower-molecular-weight products (Modified from [42]).

Processes 2025, 13, 3485 12 of 15

Although the proposed pathway is consistent with well-established degradation routes, it should be regarded as a literature-informed mechanistic hypothesis. The intermediates are representative rather than experimentally verified in this study, and no claim of complete mineralization is made. Verification would require complementary analyses such as LC–MS for organic intermediates, ion chromatography for SO_4^{2-} and small acids, TOC monitoring for mineralization degree, and radical-quenching/EPR tests to elucidate the roles of ${}^{\bullet}OH$, ${}^{\bullet}O_2^{-}$, and h^+ .

3.5. Antibacterial Properties

The results demonstrated that BiVO₄ nanoparticles exhibited a measurable antibacterial effect against *Escherichia coli* ATCC 25922, used as a model Gram-negative pathogen. After 4 h of incubation with UV-preactivated BiVO₄ nanoparticles, the number of viable bacterial cells was reduced compared to the untreated control (Figure 8). Based on colony counting from serial decimal dilutions, the bacterial concentration in the control group was 2.4×10^6 CFU/mL, while the BiVO₄-treated sample averaged 7.3×10^5 CFU/mL. This corresponds to approximately 67% inhibition, or a reduction of ~0.5 log units.



Figure 8. Photography of the TSA plate with serial dilutions of untreated *E. coli* (left) and the sample treated with UV-activated BiVO₄ nanoparticles (right).

One-way ANOVA with Tukey's test showed a statistically significant reduction in viable *E. coli* counts (p < 0.05). Although the decrease did not reach the often-cited 1-log threshold for strong antibacterial activity, UV-preactivated BiVO₄ produced a moderate, reproducible effect under ambient (non-UV) conditions, which is relevant where continuous UV exposure is impractical. The nanoscale morphology (~19 nm) and the visible-lightactive direct band gap (2.55 eV) of the synthesized monoclinic BiVO₄ promote efficient charge separation and ROS generation—features that likely underlie the observed antibacterial response [26]. This effect is plausibly mediated by nanoparticle adhesion to the bacterial envelope with ensuing membrane perturbation, aided by the high surface-area-tovolume ratio, together with oxidative stress from ROS associated with photoactive surface states. Electrostatic interactions between positively charged surface sites and the negatively charged cell envelope can further increase permeability and facilitate ROS-mediated damage to lipids, proteins, and nucleic acids, thereby reducing culturability [43]. For context, TiO₂ (P25) showed a higher E. coli reduction (~1.7 log after 180 min under visible light) compared to the present BiVO₄ system [44]. This difference primarily arises from the much stronger irradiation and more favorable reactor configuration used in that study, rather than from any intrinsic antibacterial superiority of TiO₂ under visible light. By contrast,

Processes 2025, 13, 3485 13 of 15

Ag-modified BiVO₄ commonly achieves near-complete inactivation under visible light. For example, Ag/BiVO₄ nanostructures have fully photoinactivated *E. coli* within 60 min under LED visible irradiation [45]. This superior performance is ascribed to localized surface-plasmon-assisted excitation and the role of Ag nanoparticles as electron sinks, which suppress electron–hole recombination and enhance interfacial ROS generation.

4. Conclusions

Microwave-assisted synthesis yielded phase-pure monoclinic BiVO $_4$ with nanosized (~19 nm) crystallites, a specific surface area of 7.5 m $^2/g$, and a direct band gap of 2.55 eV, enabling efficient utilization of visible light. The structural and electronic features enabled stable photocatalytic performance toward AO7 degradation, with the reaction following pseudo-first-order kinetics and achieving a degradation efficiency of approximately 77% after 120 min under visible irradiation. A moderate but statistically significant antibacterial effect was also observed under ambient, non-UV conditions, confirming the ability of UV-preactivated BiVO $_4$ to retain residual ROS activity and surface reactivity. The results demonstrate that efficient charge separation and interfacial processes can occur even at modest surface areas when crystallinity and band-gap alignment are optimized. Future work may explore Eu 3 + doping or other modifications to improve visible-light activity and charge-carrier lifetime. In addition, mechanistic analyses such as radical scavenging, EPR spectroscopy, and LC-MS/TOC measurements are recommended to verify the dominant reactive species and clarify the photocatalytic degradation mechanism.

Author Contributions: Conceptualization, D.M.; investigation, N.T. and B.V.; characterization, A.P. and I.M.; antibacterial experiments, S.D.; data curation, J.P.F.; writing—original draft preparation, N.T. and B.V.; writing—review and editing, D.M.; supervision, D.M. All authors have read and agreed to the published version of the manuscript.

Funding: This research was funded by the Ministry of Science, Technological Development, and Innovation of the Republic of Serbia, grant number 451-03-136/2025-03/200017.

Data Availability Statement: The original contributions presented in this study are included in the article. Further inquiries can be directed to the corresponding authors.

Acknowledgments: The authors are thankful to Yehezkel Yogev, Tanja Barudžija, and Dušan Mijin for providing TEM, XRD, and FTIR measurements.

Conflicts of Interest: The authors declare no conflicts of interest.

References

- Moghimi Dehkordi, M.; Pournuroz Nodeh, Z.; Soleimani Dehkordi, K.; Salmanvandi, H.; Rasouli Khorjestan, R.; Ghaffarzadeh, M. Soil, Air, and Water Pollution from Mining and Industrial Activities: Sources of Pollution, Environmental Impacts, and Prevention and Control Methods. Results Eng. 2024, 23, 102729. [CrossRef]
- 2. Shetty, S.S.; D, D.; S, H.; Sonkusare, S.; Naik, P.B.; Kumari N, S.; Madhyastha, H. Environmental Pollutants and Their Effects on Human Health. *Heliyon* **2023**, *9*, e19496. [CrossRef] [PubMed]
- 3. Tkaczyk, A.; Mitrowska, K.; Posyniak, A. Synthetic Organic Dyes as Contaminants of the Aquatic Environment and Their Implications for Ecosystems: A Review. *Sci. Total Environ.* **2020**, 717, 137222. [CrossRef]
- Slama, H.B.; Chenari Bouket, A.; Pourhassan, Z.; Alenezi, F.N.; Silini, A.; Cherif-Silini, H.; Oszako, T.; Luptakova, L.; Golińska, P.; Belbahri, L. Diversity of Synthetic Dyes from Textile Industries, Discharge Impacts and Treatment Methods. *Appl. Sci.* 2021, 11, 6255. [CrossRef]
- 5. Benkhaya, S.; M'rabet, S.; El Harfi, A. Classifications, Properties, Recent Synthesis and Applications of Azo Dyes. *Heliyon* **2020**, *6*, e03271. [CrossRef]
- 6. Kusumlata; Ambade, B.; Kumar, A.; Gautam, S. Sustainable Solutions: Reviewing the Future of Textile Dye Contaminant Removal with Emerging Biological Treatments. *Limnol. Rev.* **2024**, 24, 126–149. [CrossRef]

Processes 2025, 13, 3485 14 of 15

7. Dutta, S.; Adhikary, S.; Bhattacharya, S.; Roy, D.; Chatterjee, S.; Chakraborty, A.; Banerjee, D.; Ganguly, A.; Nanda, S.; Rajak, P. Contamination of Textile Dyes in Aquatic Environment: Adverse Impacts on Aquatic Ecosystem and Human Health, and Its Management Using Bioremediation. *J. Environ. Manag.* 2024, 353, 120103. [CrossRef]

- 8. Daneshvar, N.; Aber, S.; Hosseinzadeh, F. Study of C.I. Acid Orange 7 Removal in Contaminated Water by Photo Oxidation Processes. *Glob. NEST J.* **2008**, *10*, 16–23. [CrossRef]
- 9. Kathi, S.; El Din Mahmoud, A. Trends in Effective Removal of Emerging Contaminants from Wastewater: A Comprehensive Review. *Desalination Water Treat.* **2024**, 317, 100258. [CrossRef]
- 10. Iervolino, G.; Vaiano, V.; Pepe, G.; Campiglia, P.; Palma, V. Degradation of Acid Orange 7 Azo Dye in Aqueous Solution by a Catalytic-Assisted, Non-Thermal Plasma Process. *Catalysts* **2020**, *10*, 888. [CrossRef]
- 11. Tanos, F.; Razzouk, A.; Lesage, G.; Cretin, M.; Bechelany, M. A Comprehensive Review on Modification of Titanium Dioxide-Based Catalysts in Advanced Oxidation Processes for Water Treatment. *ChemSusChem* **2024**, *17*, e202301139. [CrossRef]
- 12. Pham, H.-C.; Kim, K.-S. Effect of TiO₂ Thin Film Thickness on NO and SO₂ Removals by Dielectric Barrier Discharge-Photocatalyst Hybrid Process. *Ind. Eng. Chem. Res.* **2013**, *52*, 5296–5301. [CrossRef]
- 13. Guo, Q.; Ma, Z.; Zhou, C.; Ren, Z.; Yang, X. Single Molecule Photocatalysis on TiO₂ Surfaces: Focus Review. *Chem. Rev.* **2019**, *119*, 11020–11041. [CrossRef]
- 14. Etacheri, V.; Di Valentin, C.; Schneider, J.; Bahnemann, D.; Pillai, S.C. Visible-Light Activation of TiO₂ Photocatalysts: Advances in Theory and Experiments. *J. Photochem. Photobiol. C Photochem. Rev.* **2015**, 25, 1–29. [CrossRef]
- Kaiba, A.; Alansi, A.M.; Oubelkacem, A.; Chabri, I.; Hameed, S.T.; Afzal, N.; Rafique, M.; Qahtan, T.F. Sunlight-Driven Synthesis of TiO₂/(MA)₂SnCl₄ Nanocomposite Films for Enhanced Photocatalytic Degradation of Organic Pollutants. *Catalysts* 2025, 15, 214. [CrossRef]
- 16. Ishigaki, T.; Nakada, Y.; Tarutani, N.; Uchikoshi, T.; Tsujimoto, Y.; Isobe, M.; Ogata, H.; Zhang, C.; Hao, D. Enhanced Visible-Light Photocatalytic Activity of Anatase-Rutile Mixed-Phase Nano-Size Powder given by High-Temperature Heat Treatment. R. Soc. Open Sci. 2020, 7, 191539. [CrossRef]
- 17. Kamble, G.S.; Natarajan, T.S.; Patil, S.S.; Thomas, M.; Chougale, R.K.; Sanadi, P.D.; Siddharth, U.S.; Ling, Y.-C. BiVO₄ As a Sustainable and Emerging Photocatalyst: Synthesis Methodologies, Engineering Properties, and Its Volatile Organic Compounds Degradation Efficiency. *Nanomaterials* **2023**, *13*, 1528. [CrossRef]
- 18. Dolić, S.D.; Jovanović, D.J.; Štrbac, D.; Far, L.D.; Dramićanin, M.D. Improved Coloristic Properties and High NIR Reflectance of Environment-Friendly Yellow Pigments Based on Bismuth Vanadate. *Ceram. Int.* **2018**, *44*, 22731–22737. [CrossRef]
- 19. Dolić, S.D.; Jovanović, D.J.; Smits, K.; Babić, B.; Marinović-Cincović, M.; Porobić, S.; Dramićanin, M.D. A Comparative Study of Photocatalytically Active Nanocrystalline Tetragonal Zyrcon-Type and Monoclinic Scheelite-Type Bismuth Vanadate. *Ceram. Int.* **2018**, 44, 17953–17961. [CrossRef]
- 20. Jeong, S.Y.; Choi, K.S.; Shin, H.-M.; Kim, T.L.; Song, J.; Yoon, S.; Jang, H.W.; Yoon, M.-H.; Jeon, C.; Lee, J.; et al. Enhanced Photocatalytic Performance Depending on Morphology of Bismuth Vanadate Thin Film Synthesized by Pulsed Laser Deposition. *ACS Appl. Mater. Interfaces* **2017**, *9*, 505–512. [CrossRef]
- 21. Jelić, S.T.; Ćirković, J.; Jovanović, J.; Novaković, T.; Podlogar, M.; Mitrić, J.; Branković, G.; Branković, Z. High Efficiency Solar Light Photocatalytic Degradation of Mordant Blue 9 by Monoclinic BiVO₄ Nanopowder. *Mater. Chem. Phys.* **2025**, 333, 130341. [CrossRef]
- 22. Regmi, C.; Dhakal, D.; Lee, S.W. Visible-Light-Induced Ag/BiVO₄ Semiconductor with Enhanced Photocatalytic and Antibacterial Performance. *Nanotechnology* **2018**, 29, 064001. [CrossRef] [PubMed]
- 23. Zhang, A.; Zhang, J. Effects of Europium Doping on the Photocatalytic Behavior of BiVO₄. *J. Hazard. Mater.* **2010**, 173, 265–272. [CrossRef]
- Drisya, K.T.; Solís-López, M.; Ríos-Ramírez, J.J.; Durán-Álvarez, J.C.; Rousseau, A.; Velumani, S.; Asomoza, R.; Kassiba, A.; Jantrania, A.; Castaneda, H. Electronic and Optical Competence of TiO₂/BiVO₄ Nanocomposites in the Photocatalytic Processes. Sci. Rep. 2020, 10, 13507. [CrossRef]
- 25. Ran, J.-H.; Fei, X.; Ni, L.; Telegin, F. Enhanced Photocatalytic Degradation of Acid Orange 7 by AgBr/BiVO₄ under Visible Light. *J. Fiber Bioeng. Inform.* **2018**, *11*, 151–161. [CrossRef]
- 26. Bulut, D.T. Exploring the Dual Role of BiVO₄ Nanoparticles: Unveiling Enhanced Antimicrobial Efficacy and Photocatalytic Performance. *J. Sol-Gel Sci. Technol.* **2025**, *114*, 198–222. [CrossRef]
- 27. Pramila, S.; Nagaraju, G.; Mallikarjunaswamy, C.; Latha, K.C.; Chandan, S.; Ramu, R.; Rashmi, V.; Lakshmi Ranganatha, V. Green Synthesis of BiVO₄ Nanoparticles by Microwave Method Using *Aegle marmelos* Juice as a Fuel: Photocatalytic and Antimicrobial Study. *Anal. Chem. Lett.* **2020**, *10*, 298–306. [CrossRef]
- 28. Marinković, D.; Righini, G.C.; Ferrari, M. Advances in Synthesis and Applications of Bismuth Vanadate-Based Structures. *Inorganics* **2025**, *13*, 268. [CrossRef]
- 29. Marinković, D.; Righini, G.C.; Ferrari, M. Synthesis, Optical, and Photocatalytic Properties of the BiVO₄ Semiconductor Nanoparticles with Tetragonal Zircon-Type Structure. *Photonics* **2025**, *12*, 438. [CrossRef]

Processes 2025, 13, 3485 15 of 15

30. Li, B.; Gao, X.; Qu, J.; Xiong, F.; Xuan, H.; Jin, Y.; Yuan, H. Visible-Light-Driven Antimicrobial Activity and Mechanism of Polydopamine-Reduced Graphene Oxide/BiVO₄ Composite. *Int. J. Mol. Sci.* **2022**, 23, 7712. [CrossRef]

- 31. Thommes, M.; Kaneko, K.; Neimark, A.V.; Olivier, J.P.; Rodriguez-Reinoso, F.; Rouquerol, J.; Sing, K.S.W. Physisorption of Gases, with Special Reference to the Evaluation of Surface Area and Pore Size Distribution (IUPAC Technical Report). *Pure Appl. Chem.* **2015**, *87*, 1051–1069. [CrossRef]
- 32. Zhang, S.-J.; Yu, H.-Q.; Li, Q.-R. Radiolytic Degradation of Acid Orange 7: A Mechanistic Study. *Chemosphere* **2005**, *61*, 1003–1011. [CrossRef]
- 33. Iqbal, N.; Huang, X.; Mohamedali Hamid, K.; Yuan, H.; Batool, I.; Yang, Y. Efficient Visible-Light-Driven Photocatalysis of BiVO₄@Diatomite for Degradation of Methoxychlor. *Catalysts* **2025**, *15*, 672. [CrossRef]
- 34. Maran, M.A.; Zheng, A.L.T.; Tan, H.Y.; Sarbini, S.R.; Tan, K.B.; Boonyuen, S.; Wong, K.K.S.; Chung, E.L.T.; Lease, J.; Andou, Y. Assessing the Photocatalytic Performance of Hydrothermally Synthesized Fe-Doped BiVO₄ Under Low-Intensity UV Irradiation. *Arab. J. Sci. Eng.* 2025, *in press.* [CrossRef]
- 35. Nunes, M.J.; Lopes, A.; Pacheco, M.J.; Ciríaco, L. Visible-Light-Driven AO7 Photocatalytic Degradation and Toxicity Removal at Bi-Doped SrTiO₃. *Materials* **2022**, *15*, 2465. [CrossRef] [PubMed]
- 36. Reza, K.M.; Kurny, A.; Gulshan, F. Parameters Affecting the Photocatalytic Degradation of Dyes Using TiO₂: A Review. *Appl. Water Sci.* **2017**, *7*, 1569–1578. [CrossRef]
- 37. Khan, S.; Noor, T.; Iqbal, N.; Yaqoob, L. Photocatalytic Dye Degradation from Textile Wastewater: A Review. *ACS Omega* **2024**, *9*, 21751–21767. [CrossRef]
- 38. Asenjo, N.G.; Santamaría, R.; Blanco, C.; Granda, M.; Álvarez, P.; Menéndez, R. Correct Use of the Langmuir–Hinshelwood Equation for Proving the Absence of a Synergy Effect in the Photocatalytic Degradation of Phenol on a Suspended Mixture of Titania and Activated Carbon. *Carbon* 2013, 55, 62–69. [CrossRef]
- 39. Phanichphant, S.; Nakaruk, A.; Chansaenpak, K.; Channei, D. Evaluating the Photocatalytic Efficiency of the BiVO₄/rGO Photocatalyst. *Sci. Rep.* **2019**, *9*, 16091. [CrossRef] [PubMed]
- 40. Mancuso, A.; Sacco, O.; Vaiano, V.; Bonelli, B.; Esposito, S.; Freyria, F.S.; Blangetti, N.; Sannino, D. Visible Light-Driven Photocatalytic Activity and Kinetics of Fe-Doped TiO₂ Prepared by a Three-Block Copolymer Templating Approach. *Materials* **2021**, *14*, 3105. [CrossRef]
- 41. Abdullahi, N.; Saion, E.; Shaari, A.H.; Al-Hada, N.M.; Keiteb, A. Optimisation of the Photonic Efficiency of TiO₂ Decorated on MWCNTs for Methylene Blue Photodegradation. *PLoS ONE* **2015**, *10*, e0125511. [CrossRef]
- 42. Viswanathan, B. Photocatalytic Degradation of Dyes: An Overview. Curr. Catal. 2018, 7, 99–121. [CrossRef]
- 43. Franco, D.; Calabrese, G.; Guglielmino, S.P.P.; Conoci, S. Metal-Based Nanoparticles: Antibacterial Mechanisms and Biomedical Application. *Microorganisms* 2022, 10, 1778. [CrossRef] [PubMed]
- 44. Haque, F.; Blanchard, A.; Laipply, B.; Dong, X. Visible-Light-Activated TiO₂-Based Photocatalysts for the Inactivation of Pathogenic Bacteria. *Catalysts* **2024**, *14*, 855. [CrossRef]
- Narváez, B.; Mendoza-Mendoza, E.; Peralta-Rodríguez, R.; Bach, H.; Barriga-Castro, E.; Segovia-Sandoval, S.; Martinez-Gutierrez, F. Visible-Leds-Induced Enhanced Photocatalytic and Antibacterial Activity of BiVO₄ Based Green Photocatalysts Decorated with Silver and Graphene. J. Photochem. Photobiol. A Chem. 2023, 447, 115191. [CrossRef]

Disclaimer/Publisher's Note: The statements, opinions and data contained in all publications are solely those of the individual author(s) and contributor(s) and not of MDPI and/or the editor(s). MDPI and/or the editor(s) disclaim responsibility for any injury to people or property resulting from any ideas, methods, instructions or products referred to in the content.